

Lithology-derived structure classification from the joint interpretation of magnetotelluric and seismic models

P. A. Bedrosian,^{1*} N. Maercklin,² U. Weckmann,¹ Y. Bartov,³ T. Ryberg¹ and O. Ritter¹

¹GeoForschungsZentrum Potsdam, Telegrafenberg, D-14473 Potsdam, Germany

²RISCC, University of Naples, Via Coroglio 156, 80124 Napoli, Italy

³Geological Survey of Israel, Malchei Yisrael St. 30, 95501 Jerusalem, Israel

Accepted 2007 March 13. Received 2007 January 8; in original form 2006 March 29

SUMMARY

Magnetotelluric and seismic methods provide complementary information about the resistivity and velocity structure of the subsurface on similar scales and resolutions. No global relation, however, exists between these parameters, and correlations are often valid for only a limited target area. Independently derived inverse models from these methods can be combined using a classification approach to map geologic structure. The method employed is based solely on the statistical correlation of physical properties in a joint parameter space and is independent of theoretical or empirical relations linking electrical and seismic parameters. Regions of high correlation (classes) between resistivity and velocity can in turn be mapped back and re-examined in depth section. The spatial distribution of these classes, and the boundaries between them, provide structural information not evident in the individual models. This method is applied to a 10 km long profile crossing the Dead Sea Transform in Jordan. Several prominent classes are identified with specific lithologies in accordance with local geology. An abrupt change in lithology across the fault, together with vertical uplift of the basement suggest the fault is sub-vertical within the upper crust.

Key words: electrical resistivity, geostatistics, magnetotellurics, seismic structure, seismic velocity, tomography.

1 INTRODUCTION

The interpretation of geophysical models derived by inversion is a highly subjective part of any geologic study. Our incomplete knowledge of the subsurface, the spatially-varying resolution of the models, and the non-uniqueness of the geophysical inverse problem make it difficult to objectively interpret physical property models in terms of geologic structure. The problem is exacerbated by the many-to-many, or at best, many-to-one, relationship between geologic units and their physical properties. It is thus commonplace to use multiple methods to determine multiple physical properties over an area of interest in order to discriminate between the range of possible geologic/lithologic structures. The analysis of such complementary data, however, is rarely taken beyond a qualitative comparison. Attempts at a quantitative comparison are, for the most part, centered upon constitutive or empirical relations between physical properties, which tend to be limited in scale and applicability.

Seismic and magnetotelluric (MT) methods are often favored for crustal studies as they provide images of acoustic velocity (V_p , V_s)

and electrical resistivity (ρ), respectively, on similar scales and with comparable spatial resolution (Jones 1987). By looking in tandem at velocity and resistivity we retain the strengths of each method, while lessening the susceptibility of our interpretation to their individual weaknesses. Seismic refraction, for example, has difficulty imaging vertical velocity contrasts. Along a similar vein, MT has difficulty resolving structure beneath strong conductors due to the large amount of energy dissipated within them. A properly formulated joint interpretation must take these variations in resolution into account, but unfortunately there exists no fundamental law linking resistivity and velocity. The reason for this is that electrical resistivity is most sensitive to minor fluid phases within a rock, while acoustic velocity is equally sensitive to the rock matrix. This does not suggest these methods are discordant, but rather that empirical relations between ρ and V_p at best hold locally, within a specific lithology. A joint statistical interpretation can describe the correlation between these physical parameters without imposing unrealistic empirical constraints.

The methodology we explore is sketched in Fig. 1. Coincident and independently-derived velocity and resistivity models are first interpolated onto a common grid. We stress that an inversion model can be thought of as an ensemble of point values, each associated with a particular location. Interpolating onto a common grid thus results in a set of co-located model points, each identified with a velocity,

*Now at: US Geological Survey, MS 964, Box 25046, Denver, CO, 80225, USA. E-mail: pbedrosian@usgs.gov

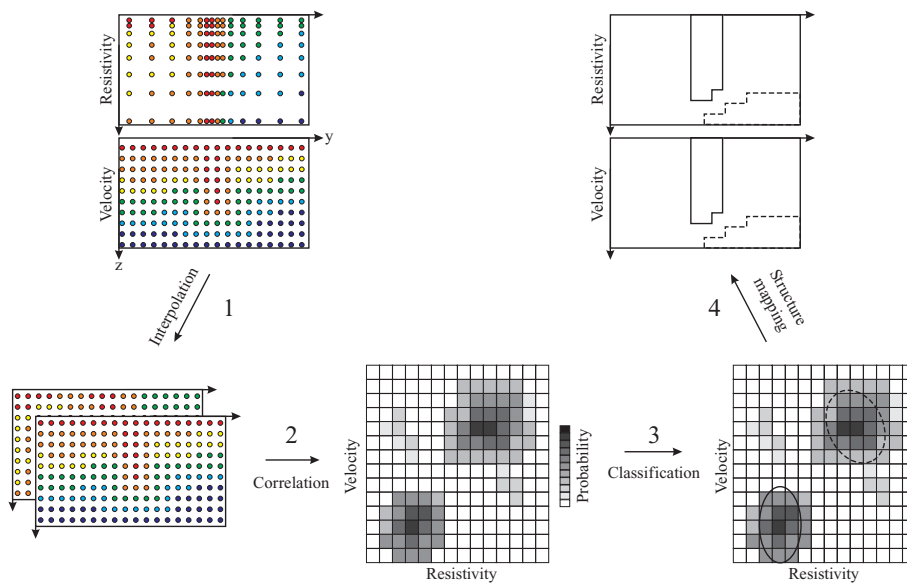


Figure 1. Probabilistic approach to structure classification using independent geophysical models. Independent models are first interpolated onto a common grid. The correlation between the models is subsequently examined and significant classes (localized regions of high correlation) are identified. Classes are finally mapped back into onto the depth section.

resistivity, and spatial location. Together with error estimates of the model parameters at each location, a probability density function (pdf) is assembled in the joint parameter space. Classes are subsequently identified as localized regions of enhanced probability density and finally mapped back to the spatial domain (a depth section) where their locations define geologic structures (under certain assumptions to be discussed later). Our methodology is based on a probabilistic approach developed by Bosch (1999). While this work was aimed at joint inversion, we represent the plural geophysical data as a pdf in the joint parameter space, in an analogous fashion to this earlier work. This approach has been applied to lithology classification, in particular by Bauer *et al.* (2003), who examined models of seismic velocity and Poisson's ratio, linking the resulting classes to geologic structure through petrological constraints.

More commonly, scatterplots of independent physical property models are examined, such as a study by Haberland *et al.* (2003b) which combined models of electrical resistivity and seismic attenuation to define regions of partial melting within the Altiplano plateau. Bedrosian *et al.* (2004) applied a similar method to seismic and MT models of the San Andreas Fault, delineating several tectonic and hydrologic boundaries. These studies, however, are rather *ad hoc* in their approach to classification and furthermore treat all data equally, i.e. they ignore the effects of spatially-varying model resolution.

Maercklin (2004) similarly used scatterplots of resistivity and seismic velocity to delineate lithologic structure surrounding the Dead Sea Transform (DST). This work was subsequently integrated with seismic scattering studies to characterize the DST in the near surface (Maercklin *et al.* 2005). These preliminary studies are the motivation for the present work. Using coincident geophysical models crossing the Dead Sea Transform in Jordan, this paper develops a statistically-robust framework to extract structural information from seismic and electric data. This approach fills a gap between qualitative comparison of independent models and joint inversion of the underlying data (Bedrosian 2007); it is more rigorous than the former and can be applied to existing models without renewed inversion of the data. Furthermore, this work addresses topics which

arise in all joint geophysical inversions based on model structure linkages (Haber & Oldenburg 1997; Gallardo & Meju 2003, 2004, 2007; Linde *et al.* 2006).

2 BACKGROUND AND MODELS

The left-lateral Dead Sea Transform (DST) accommodates the relative motion of the Arabian and African plates, stretching over 1000 km between the Taurus collision zone in the north and the Red Sea rift in the south (inset, Fig. 2). The DST fault system has a Holocene slip rate of 4 ± 2 mm yr⁻¹, and is estimated to have accumulated ~105 km of sinistral offset since its formation around 17–22 Ma (Niemi *et al.* 2001; Klinger *et al.* 2000; Garfunkel *et al.* 1981; Bartov *et al.* 1980; Freund *et al.* 1970). Aside from a compressional period in the late Cretaceous (Syrian Arc phase, Bosworth *et al.* 1999), the region has remained stable since the early Mesozoic. Recent seismic activity is concentrated along the DST, and to a minor extent on the Central Negev Shear Zone (van Eck & Hofstetter 1990). Seismicity along the southern DST is most pronounced near tensional features such as the Dead Sea and the Gulf of Aqaba/Elat, though large historical earthquakes have occurred along the length of the fault system (Amiran *et al.* 1994; Klinger *et al.* 2000).

Basement in the region consists of late Proterozoic rocks comprising the Arabo-Nubian Shield (Stern 1994; Stoeser & Camp 1985; Bender 1968). A succession of Late Precambrian volcano-sedimentary sequences overlie the basement throughout much of the region with significant variations in thickness and coverage (Weissbrod & Sneh 2002). Phanerozoic cover is predominantly Cretaceous and Tertiary, underlain in places by Jurassic, Triassic, and Permian sequences. To the east of the DST, these latter sequences are generally absent, and Cretaceous rocks lie unconformably upon sandstones of Ordovician and Cambrian age.

As part of the DESERT project, geological and geophysical data were acquired along a profile centered on the DST, traversing Israel and Jordan (Weber *et al.* 2004; DESERT Research Group 2000). The profile crossed the Araba/Arava Fault (AF), locally the

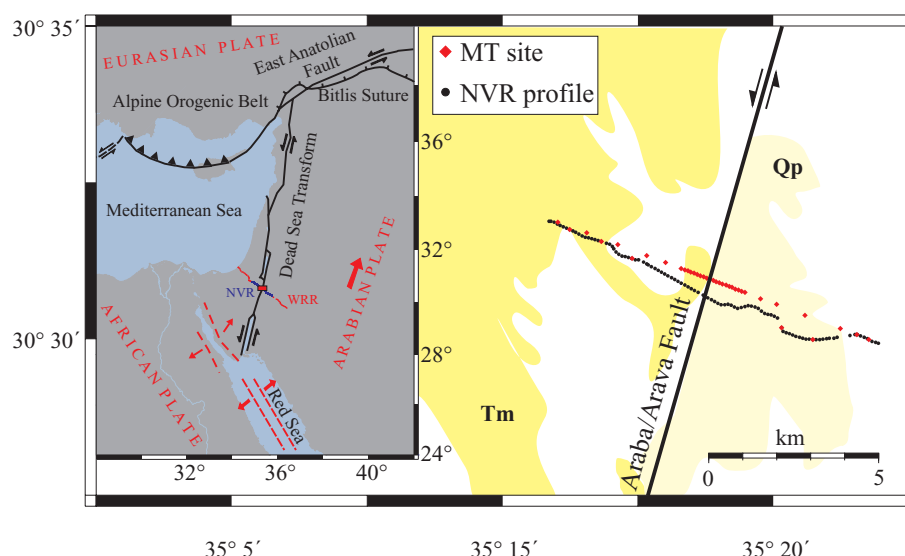


Figure 2. Site location map for the area of study (small red rectangle on the inset regional tectonic map). WRR = Wide-angle reflection/refraction profile; NVR = Near-vertical reflection profile. MT site locations in main figure denoted by red diamonds; Black dots represent vibroseis source points along the NVR profile. Surface geology consists of Quaternary alluvium except as marked. Qp, Quaternary sand dunes; Tm, Miocene Hazeva Fm.

expression of the DST, within the Araba/Arava Rift midway between the Dead Sea and the Gulf of Aqaba/Elat (inset, Fig. 2). Geophysical studies included a 100 km near-vertical-incidence reflection (NVR) experiment, a 260 km wide-angle reflection/refraction experiment, and a 150 km magnetotelluric transect. This study is concerned with the innermost 10 km of the profile across the AF, focusing on the coincident MT and NVR data.

2.1 Magnetotelluric modelling

Magnetotelluric data were first acquired in 2000 with sites spaced every 100 m in the vicinity of the Araba/Arava Fault, expanding to every 500 m at the profile ends (Fig. 2). Measurements were made using GPS synchronized SPAM MkIII instruments (Ritter *et al.* 1998), which recorded electric and magnetic field variations for a duration of 2 days. Vertical magnetic fields were recorded at all sites in addition to traditional (horizontal field) MT data in order to further constrain subsequent inversion. MT and vertical-field transfer functions were estimated within the frequency range of 1000–0.001 Hz using processing techniques described in Weckmann *et al.* (2005). Dimensionality analysis was carried out via examination of skew, geoelectric strike, and induction vectors, which all confirm that the measured data are in accordance with the predominantly 2D geologic structure defined by the Araba/Arava Fault (Ritter *et al.* 2003).

Upon rotation into a fault-aligned coordinate system ($N18^\circ E$), data modelling and inversion were carried out using the Winglink analysis package (<http://www.geosystem.net>). The 2D regularized inversion algorithm of Rodi & Mackie (2001) was employed to produce potential models spanning a range of regularization parameters and data error floors. Models were subsequently refined based on their common characteristics and agreement with the measured data. The model shown in Fig. 3(a) is derived from a uniform resistivity starting model ($50 \Omega m$) and fits the MT and vertical-field data to a combined r.m.s. error of 2.1, a 600 per cent reduction in error from that of the starting halfspace model.

As all parts of the final inverse model are not equally resolved, estimates of the errors in the individual model parameters are needed.

In magnetotellurics, the pairwise sensitivity of each model parameter to each datum is contained within the Jacobian of the linearized forward problem, typically termed the sensitivity matrix. Schwalenberg *et al.* (2002) suggest using normalized averages of the sensitivity matrix to assess the relative sensitivity of individual model parameters. This method in effect calculates the average sensitivity of a given model parameter to all the measured data, normalized by the measurement error in each datum. This linear sensitivity analysis (only accounting for small perturbations of the model) has been used to estimate resistivity errors according to:

$$\delta_{\log(\rho),i} = C_{\log(\rho)} \cdot \left[\frac{\log(s)}{\log(s_i)} \right], \quad (1)$$

where s_i is the normalized sensitivity of a given cell, and $C_{\log(\rho)}$ is the mean error in $\log(\rho)$, a constant to be determined. The overline indicates an average over all model points.

2.2 Seismic modelling

The near-vertical-incidence reflection experiment was carried out in 2000 using vibroseis trucks as seismic sources. An 18 km recording spread (180 geophones) was moved along the 100 km profile in split-spread configuration. An additional 86 seismic stations remained fixed along the profile for the duration of the survey. 280, 335 direct P -wave arrival times were manually picked from the subsequent data and inverted using the two-dimensional (2D) FAST code of Zelt & Barton (1998). Travel time picks have been used to construct a set of best fitting one-dimensional (1D) models, which were stitched together and used as the starting model for the 2D inversion. The final inversion mesh consists of blocks 100 m wide and 50 m thick. The shallow parts of the model (upper 5 km) generally have high ray coverage, and hence are well-constrained by the data. The robustness of the final model (innermost 10 km shown in Fig. 3c) was confirmed by testing the stability of model features while varying smoothness constraints, regularization parameters, starting models, mesh gridding, and mesh location. An iterative inversion approach led to a final velocity model independent of the

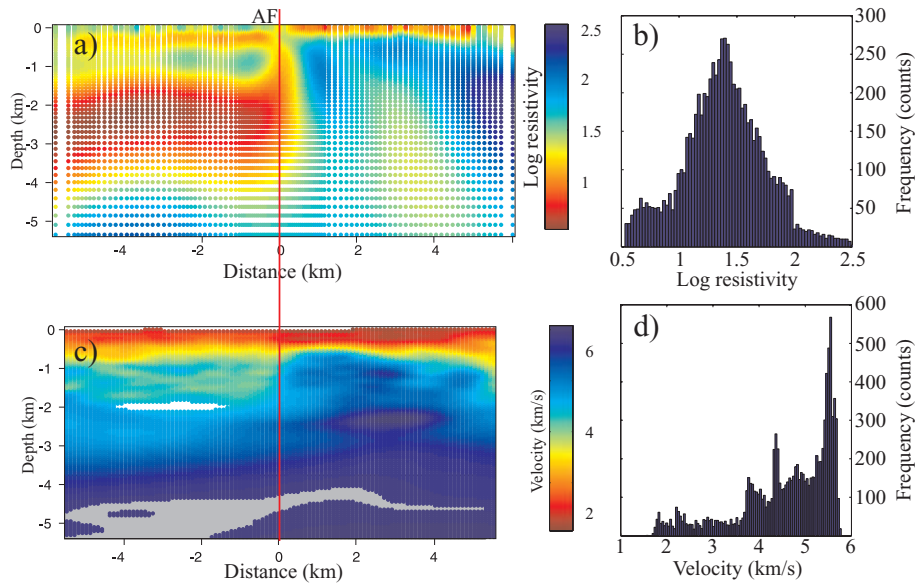


Figure 3. Independent resistivity (a) and velocity (c) models selected for joint interpretation. Histograms of model resistivities and velocities (initial point distributions, IPD) shown in (b) and (d), respectively. Models are only considered from the surface to 5 km depth due to decreasing resolution at greater depths. The resistivity model was calculated on a non-uniform mesh of 5136 cells, while the velocity model was calculated on a uniform mesh of 10 000 cells. The white area of the seismic model is where ray coverage was too sparse to constrain velocities; gray area denotes a region where starting-model velocities were unaffected by inversion. The red line marks the surface trace of the Arava/Arava Fault (AF).

starting velocity model. An exception is the narrow strip within the model (gray area in Fig. 3c) where velocities remained unchanged (to two decimal places) during the inversion; model parameters in this strip were removed from subsequent analysis as they represent velocities unconstrained by the data. A final r.m.s. travel time misfit of 0.045 s was achieved.

Checkerboard tests suggest the model resolution is better than 200 m in the upper 1 km, decreasing to ~ 500 m at 2 km depth. The relative velocity errors are estimated from ray coverage. A mean velocity error, C_{V_p} , remains to be determined. Velocity errors are estimated as:

$$\delta_{v_p,i} = C_{V_p} \cdot \left[\frac{\overline{\log(n)}}{\log(n_i)} \right], \quad (2)$$

where n_i is the number of hit counts in a given cell and the overline indicates an average over all model points.

3 ANALYSIS

3.1 Interpolation

In order to examine the correlation between the models shown in Fig. 3, physical property values must be estimated at a common set of grid points. This procedure will generally involve both projection and interpolation, though in our case projection is unnecessary, as sites were projected onto a common profile prior to inversion. Interpolation, specifically point estimation, can be performed in a variety of ways, the details of which are covered in standard geostatistical texts (Isaaks & Srivastava 1989; Armstrong 1998). What is important to any interpolation method is that the estimated and original point distributions are statistically similar. Recall that each model can be viewed as an ensemble, or distribution of point values as emphasized in the presentation of Fig. 3. For our purposes, it is also important to consider the size (number of model points) within the initial and estimated distributions as well as the spatial uniformity

of the final interpolated models. The former should be maximized to provide better statistics, while the latter will influence the relative weighting of various parts of the model.

A fundamental difference between electric and seismic tomography methods is the discretization of the model mesh or grid. Though a uniformly-spaced grid is commonly used during seismic inversion, the physics of the MT problem, in which energy dissipates exponentially with distance inside the earth (e.g. Vozoff 1987), demands a non-uniform model grid that progressively coarsens with both depth and distance from the measurement sites. In arriving at a common grid, one can:

- (i) estimate resistivity values at each velocity grid point,
- (ii) estimate velocity values at the resistivity grid point, or
- (iii) interpolate both resistivity and velocity values onto an independent set of grid points.

Choices 1 and 2 result in significantly different estimated point distributions (EPD) due to differences in the sizes of the initial point distributions (IPD). As the velocity model contains more mesh points than the resistivity model, choice 2 ($V_p \rightarrow \rho$) results in a net loss of velocity information, while choice 1 ($\rho \rightarrow V_p$) preserves the information content of both models. Concerning spatial uniformity, choice 1 (2) results in an EPD that is spatially uniform (non-uniform). For subsequent correlation, we require a uniform distribution to ensure that all parts of the model are equally represented.

A final consideration is that all interpolation methods, by averaging several point values to form an estimate, produce an EPD that is smoother (reduced variance) than the IPD. As our final goal is to identify geologic structures by their different physical properties, this smoothing masks the differences we seek. Keeping the number of interpolations to a minimum is desired, and for this reason, choice 3, in which both data sets are interpolated, is not considered. We proceed with interpolating the resistivity mesh onto the velocity mesh (choice 1).

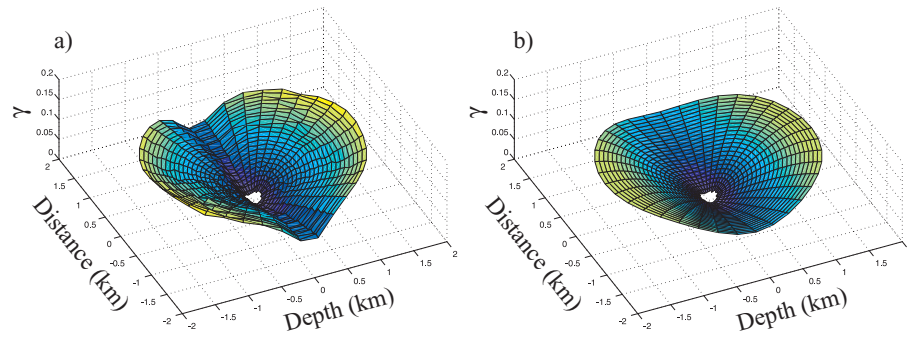


Figure 4. Experimental (a) and modelled (b) variograms for the resistivity model in Fig. 3(a). Experimental variogram exhibits geometric anisotropy, in which model structures are more continuous along the profile than with depth. Modelled variogram is the result of a three parameter fit to a spherical function.

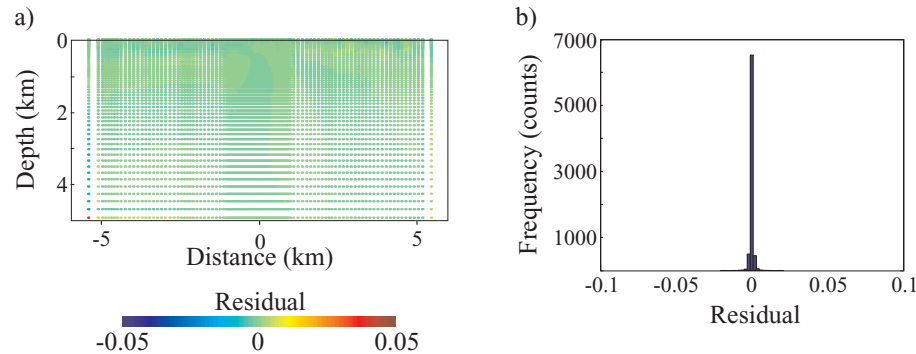


Figure 5. Cross-validation study. Spatial (a) and ordinary (b) distribution of resistivity residuals (original minus estimated resistivity) for ordinary kriging. Red (blue) regions of the cross-section have resistivities underestimated (overestimated) by the interpolation.

Point estimation, or interpolation was done using ordinary kriging (OK). OK forms estimates from a weighted average of many samples; sample weights take into account both the spatial clustering of the samples (in our case the IPD of the resistivity model) and the spatial continuity of the sample values (resistivity). As such, OK produces an estimated point distribution whose residuals (as determined by cross-validation) have zero mean and minimum variance.

OK requires a model of spatial continuity for the property to be interpolated (resistivity). This spatial continuity is expressed by the experimental variogram, a directionally-dependent function which must be calculated and modelled (Isaaks & Srivastava 1989). Fig. 4(a) illustrates the experimental variogram of the resistivity model. The lack of azimuthal symmetry in the experimental variogram is indicative of geometric anisotropy, with greater spatial uniformity along profile than with depth. This is not unexpected, as geologic structures, and by inference their defining physical properties, are typically areally expansive, yet often quite thin. Put simply, lithologies can stretch for hundreds or even thousands of kilometers, but are seldom more than a few kilometers thick. The short-offset (0–1.5 km) experimental variogram was fit to a three parameter spherical function model; the resulting best-fit variogram can be seen in Fig. 4(b) for comparison. This modelled variogram was subsequently incorporated into the ordinary kriging procedure to derive resistivity estimates at each of the velocity mesh points. OK was applied in an analogous manner to derive resistivity errors for the EPD.

The accuracy of the interpolated resistivity model is evaluated through cross-validation. A form of jack-knife estimation, cross-validation builds an estimated point distribution by removing a sample from the IPD and using the remaining samples to estimate it as

if it were missing. In this manner, a residual between the IPD and EPD can be calculated. The spatial and ordinary distribution of the residuals are shown in Figs 5(a) and (b), respectively, and indicate little deviation between the IPD and EPD.

The relationship between resistivity and velocity can be examined using quantile-quantile (QQ) plots, a measure of the statistical similarity between two distributions (Isaaks & Srivastava 1989). Plotted for the initial resistivity and velocity distributions (Fig. 6a), the QQ plot is linear except at high values of ρ/V_p , suggesting strong similarity. Post-interpolation, the ρ/V_p relationship (Fig. 6b) is changed somewhat due to differences in the initial and estimated resistivity distributions. In particular, the differences reflect the spatial uniformity of the resistivity grid. The non-uniform IPD disproportionately weights shallow structure, in contrast to the uniform grid of the EPD.

3.2 Model correlation

Having arrived at a common point distribution, we turn our attention to the correlation of the resistivity and velocity models. While QQ plots examine the ρ/V_p distributions as a whole, scatterplots (Fig. 7a) present a point-by-point examination of model correlation. Correlation is evident from the spatial clustering of the model points in the joint parameter space, however no clear global relation is observed. This is in contrast to the work of Dell'Aversana (2001), where scatterplots from a collection of borehole data define a simple curve relating resistivity to velocity. A series of arcuate tracks in Fig. 7(a) form a fine-scale 'structure' within the scatterplot, each track representing a vertical or horizontal slice through the model section. These tracks are a result of both the periodicity of the model

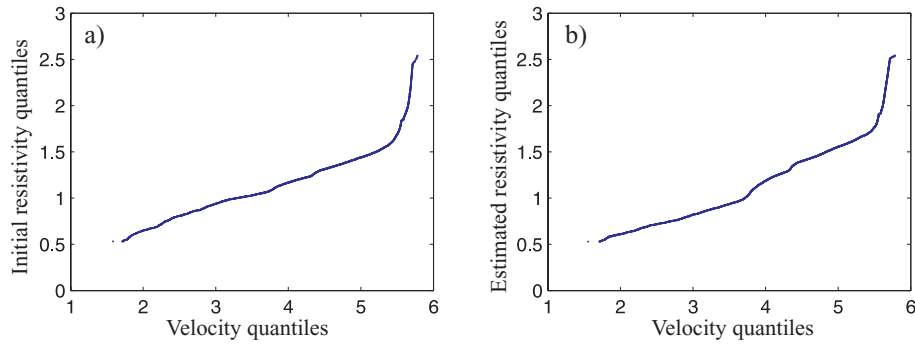


Figure 6. Comparison of model distributions. (a) Quantile-quantile plot of initial resistivity and velocity distributions. (b) Quantile-quantile plot of the estimated resistivity distribution and velocity distribution. Similarity of the two plots suggests the interpolation procedure has not significantly altered the resistivity/velocity relationship.

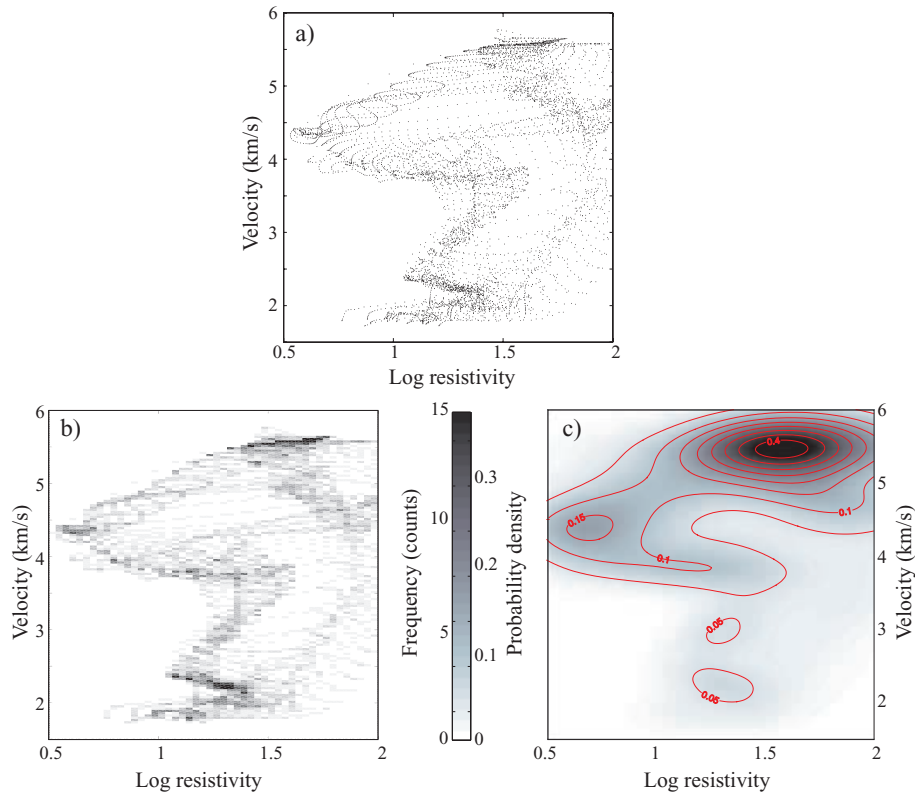


Figure 7. Correlation of seismic velocity and electrical resistivity in parameter space. (a) Scatter plot of velocity versus log resistivity for the estimated point distribution. (b) Correlation obtained upon binning the EPD. (c) Correlation viewed as the joint probability density function of the EPD, taking into account errors in the model parameters. Contour interval is 0.05.

grid and the smoothing enforced by the inversion. The differences $\Delta \log(\rho)$ and ΔV_p between tracks are on average less than 0.1 and 0.1 km s⁻¹, respectively, providing estimates of discretization error. We have used these values to set the mean errors, $C_{\log(\rho)}$ and C_{V_p} , in eqs (1) and (2), respectively.

In order to identify classes (regions of high correlation, and by inference well-defined physical properties), the distribution was binned to produce the histogram in Fig. 7(b). Binning averages out some of the distracting fine-scale structure in the scatterplot (Fig. 7a), however the creation of the histogram requires a choice of bin size (here $\Delta \log(\rho) = 0.03$, $\Delta V_p = 0.03$ km s⁻¹), which introduces additional subjectivity into the process. Furthermore, there is no straightforward way in which to incorporate the errors in re-

sistivity and velocity model values into the histogram. Though this approach has been employed by Maercklin (2004) and Bedrosian *et al.* (2004), here we pursue a probability density approach which does not suffer these limitations (Schalkoff 1992).

Each element of our point distribution can be viewed as a measure or outcome of a process defined by a probability density function (pdf). Assuming the data (the collection of model points) are independent, a joint pdf describes the full distribution and can be expressed as a sum of the probability density functions for each datum (eqs 3, 4). Assuming a normal error distribution, the pdf for the i th data point can be expressed as a function of velocity and resistivity, where $\delta \log(\rho_i)$ and $\delta V_{p,i}$ are the errors defined in eqs (1) and (2), and n is the total number of data points. The joint pdf

(Fig. 7c) can be compared to the histogram in Fig. 7(b); broad-scale similarities can be seen.

$$\text{pdf}(\rho, v_p) = \frac{1}{n} \sum_{i=1}^n \text{pdf}_i(\rho, v_p) \quad (3)$$

$$\text{pdf}_i(\rho, v_p) = \frac{1}{\sqrt{2\pi\delta\log(\rho_i)\delta V_{p,i}}} \times \exp -\frac{1}{2} \left[\frac{(\log(\rho) - \log(\rho_i))^2}{\delta\log(\rho_i)^2} + \frac{(V_p - V_{p,i})^2}{\delta V_{p,i}^2} \right] \quad (4)$$

3.3 Classification

In the previous section we calculated the joint pdf describing the data set, taking into account error distributions in both resistivity and velocity. We proceed under the assumption that lithotypes are spatially-connected domains characterized by uniform physical properties which are normally distributed about a mean. It is possible to identify lithotypes from the joint pdf, provided the contrast in physical properties between lithotypes is greater than their estimated errors. Practically, this amounts to being able to separate overlapping peaks in the joint parameter space. An examination of the pdf (Fig. 7c) reveals several regions of enhanced probability density connected to one another via linear ‘bridges’ in parameter space. Were the MT and seismic models completely uncorrelated, the resulting pdf would be structureless (uniform, flat probability density). The task is thus to extract a series of classes (inferred to represent lithotypes under the assumption above) from the calculated joint pdf. The problem of classification reduces to the following questions: how many statistically significant classes exist, how can they be defined, and how do we determine class inclusion for a given datum?

A hybrid of two classification approaches is pursued. In the first approach, classes and their boundaries are manually chosen from the joint pdf (Fig. 8a). In the second, a non-linear least-squares fitting routine is used to determine the location and extent of classes in parameter space. The first method, though subjective, allows for an interactive examination of class structure in both the parameter and spatial domains. Insight from this manual examination is subsequently used to constrain the fitting routine, permitting a statistical

rather than subjective definition of class boundaries. In effect, this hybrid method forces the fitting algorithm toward local, rather than global fitting of the joint pdf, permitting cleaner class separation, and as will be shown, results in classes that are more realistically distributed in depth section.

Levenberg-Marquardt least-squares optimization was used to fit the joint pdf as a sum of bivariate Gaussian functions (eq. 5):

$$f(\mathbf{x}) = \sum_i^n \frac{a_i}{2\pi|\Sigma_i|^{1/2}} \exp -\frac{1}{2} [(\mathbf{x} - \mu_i)^T \Sigma_i^{-1} (\mathbf{x} - \mu_i)], \quad (5)$$

where $\mathbf{x} = [\log(\rho), V_p]$. This non-linear, parametric estimation technique determines the amplitude, a_i , mean, μ_i , and covariance, Σ_i , for the n Gaussian functions (classes) that best fit the joint pdf. The number of classes are supplied by the user, as well as initial guesses for the $6 * n$ fit parameters. The convergence of this iterative fitting algorithm is sensitive to the starting parameter values, and for a complicated pdf will rarely converge to a solution given randomly-chosen starting values. As such, initial class amplitudes, means, and covariances were chosen close to their assumed values, as determined during the manual class selection. Constraints were further placed on the range of certain parameters to enforce the shape or location of classes in parameter space. Where closely spaced, class means were fixed at their starting values. All of these constraints serve to steer the global fitting algorithm toward local structure and aid in peak separation.

The optimum number of classes was determined from examination of global misfit as a function of the number of classes fit. The ‘knee’ of the resulting L-curve (Fig. 9a), though not pronounced, occurs between 4 and 7 classes, beyond which the introduction of more classes does not significantly lower the misfit. The final choice of 6 classes stems from examination of the distribution of classes in depth section. It was found that beyond 6 classes, the spatial connectivity of classes began to falter, suggesting that lithotypes are being split among multiple classes. The best 6 class fit to the joint pdf is shown in Fig. 8(b). The misfit between the calculated and modelled pdf is shown in Fig. 9(b) and illustrates the quality of the fit in different regions of parameter space.

Class boundaries are defined by confidence intervals for the 6 Gaussian peaks, as illustrated in Fig. 8(b). It is important to avoid overlap between classes boundaries lest the question of a datum’s class inclusion become ambiguous. The confidence intervals have

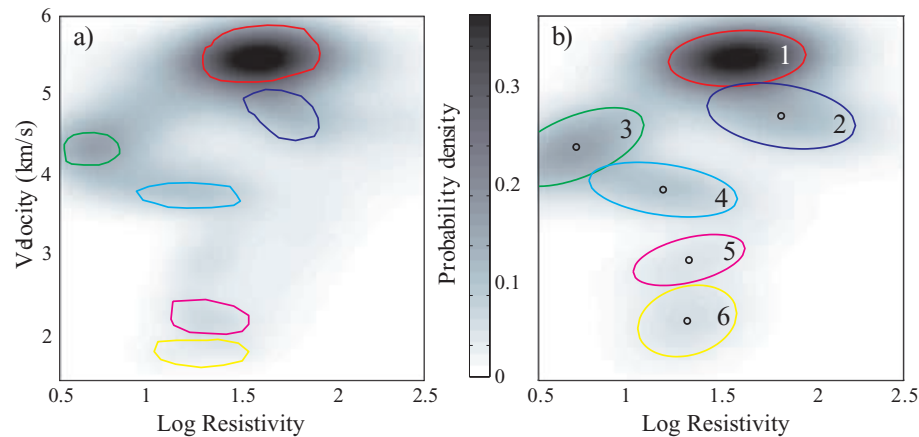


Figure 8. Manual (a) and hybrid (b) class selection. Class boundaries are overlain upon the calculated and modelled pdfs in (a) and (b), respectively. Black circles in (b) denote the mean class values and colored ellipses the ~60 per cent confidence interval for each of the peaks used to fit the calculated pdf. Manual class selection was undertaken to interactively investigate the correlation of resistivity and velocity both in parameter space and in depth section (Fig. 10a). Results were subsequently used to constrain certain parameters within the hybrid fitting routine.

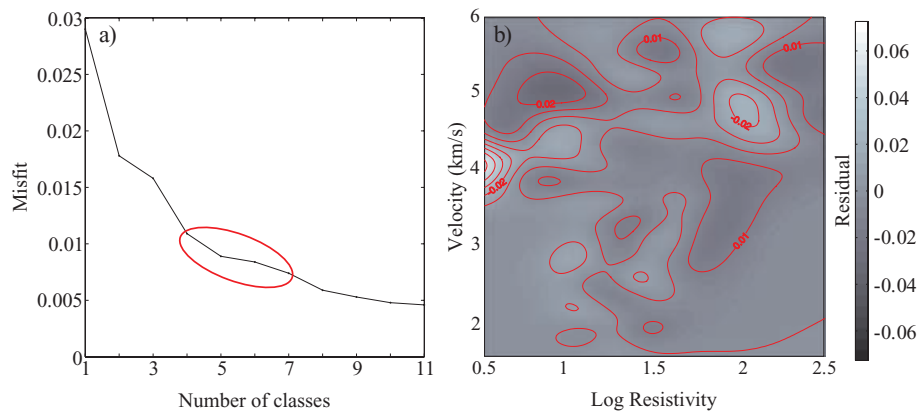


Figure 9. (a) L-curve of fit residual versus number of classes. Red oval denotes the optimal trade-off between misfit and number of classes. (b) Residual between calculated pdf and six-class modelled pdf shown in Figs 8(a) and 8(b), respectively. Contour interval is 0.01

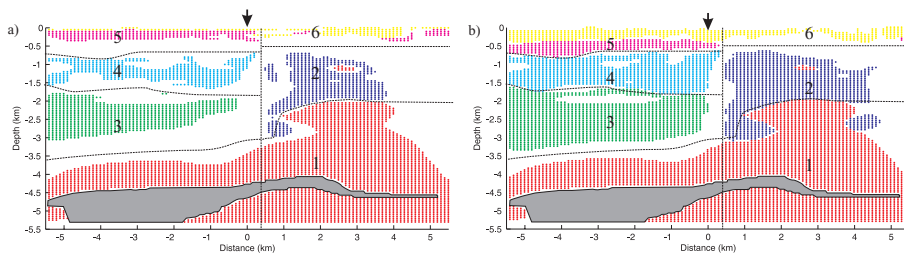


Figure 10. Spatial distribution of classes derived from manual classification (a) and a hybrid fitting routine (b). Colors correspond to the those of the class boundaries defined in Fig. 8. Arrows mark the surface trace of the Araba/Arava Fault and dashed lines highlight the boundaries identified. Gray region indicates missing data in the initial seismic velocity model.

been selected as the full-width, half-maximum (FWHM) value of each fitted peak. Defining class boundaries in this fashion leads to minimal overlap, with 76 per cent of the EPD falling within one of the 6 classes, and less than 0.2 per cent of these falling into overlapping classes. As opposed to defining class boundaries along a probability density contour, this choice accounts for variations in peak amplitude which in turn reflect the differing spatial extent (cross-sectional area) from which each class derives. As chosen, the class boundaries represent ~ 60 per cent confidence intervals, though these are upper bounds derived not from the class boundaries themselves, but from rectangular regions enclosing them.

Mapping back to a depth section, Fig. 10 illustrates the spatial distribution of class boundaries picked manually (a) and through the hybrid fitting routine (b). Note the similarity between the distributions, indicating the robustness of the method to how class boundaries are chosen. The highlighted classes for the most part define spatially connected regions, verifying an earlier assumption and suggesting the classes define distinct earth structures. The subhorizontal class boundaries, together with their significant along-profile extent, further suggest they represent distinct lithotypes. Four of the six classes are abruptly terminated across a vertical boundary in close proximity to the surface trace of the Araba/Arava Fault. The slight irregularity within the fault zone may be attributed to secondary minor faults in close proximity to the major fault.

The imaged classes and their boundaries represent a combination of the structure in the initial models (Figs 3a, c). The top boundaries of classes 1, 2 and 4 are primarily derived from the seismic model, while those for classes 3 and 5 are most clearly imaged by the MT model. Furthermore, the sharp vertical discontinuity bounding classes 2–5 is most evident in the MT model. It would be difficult

to define the lithology of Fig. 10 from either of the two starting models.

4 DISCUSSION

4.1 Imaged structure

Table 1 enumerates the classes defined in Fig. 10 and their ranges in resistivity, velocity and thickness. With the exception of classes 1 and 6, all classes are truncated at a vertical boundary, a not unexpected result given up to 60 km of post Miocene sinistral off-set (Kesten *et al.* 2007) on the Araba/Arava Fault. Classes 1 and 2 are characterized by high velocity and moderate resistivity, typical of igneous or metamorphic rocks, but less common for the sedimentary rock found locally, composed of alternating layers of sandstone and carbonate rock with considerable amounts of clay and marl. These classes furthermore correspond spatially to deeper parts of the model, suggesting they may reflect basement rocks of the Arabo-Nubian shield (Ibrahim & McCourt 1995). In contrast, classes 5 and 6, with low velocity and resistivity, can only be attributed to sedimentary rock, and are structurally the highest units in the section. Class 4, with $V_p = 3.9 \pm 0.3 \text{ km s}^{-1}$ and $\rho = 6 - 39 \Omega \text{m}$, is typical of clastics or consolidated sediments, and is at sufficient depth to have undergone compaction. Class 3 is enigmatic as it is characterized by moderate velocity, similar to class 4, but extremely low resistivity, lower even than the surface sediments.

Together with regional stratigraphy, and based on the determined velocity/resistivity values, classes have been associated with specific

Table 1. Resistivity, seismic velocity, and thickness (t) of classes denoted in Fig. 10. Also included are inferred age, rock type, and geologic unit based on constraints discussed in the text. Classes spanning the Araba/Arava Fault are identified by geologic unit on both the west (W) and east (E) sides of the fault.

Cls.	ρ ($\Omega \cdot m$)	V_p ($km\ s^{-1}$)	t (km)	Age	Lithology type	Stratigraphic unit
1	16 – 92	5.5 ± 0.3	1.5+	/PC	ark., cgl., volc.	Zenifim fm.(W); Aqaba cmplx.: Ghuwayr volc., Araba cmplx. (undif.)(E)
2	26 – 173	4.8 ± 0.4	3+	/PC	cgl., qtz. porph.	Fidan grnt., Araba cmplx.: Ahaymir volc.(E)
3	2 – 11	4.4 ± 0.5	1.6	C-K	sst., lst., dolm., mar., clst.	Yam Suf, Negev, Ramon, Kurnub, Judea grs(W) ~ 1.7 km
4	6 – 39	3.9 ± 0.3	1.0	/K-T	chk., cht., lst. mar.	Mt. Scopus, Avedat grs.(W)(equiv. to Belqa gr.), 700 m
5	10 – 43	3.0 ± 0.3	0.5	Tm	sst., clst., cgl.	Hazeva gr.(W) ~ 500 m
6	11 – 39	2.2 ± 0.4	0.2	Tp-Qp	alluv: cgl., sd., slt., grvl.	Arava fm.(W, E)

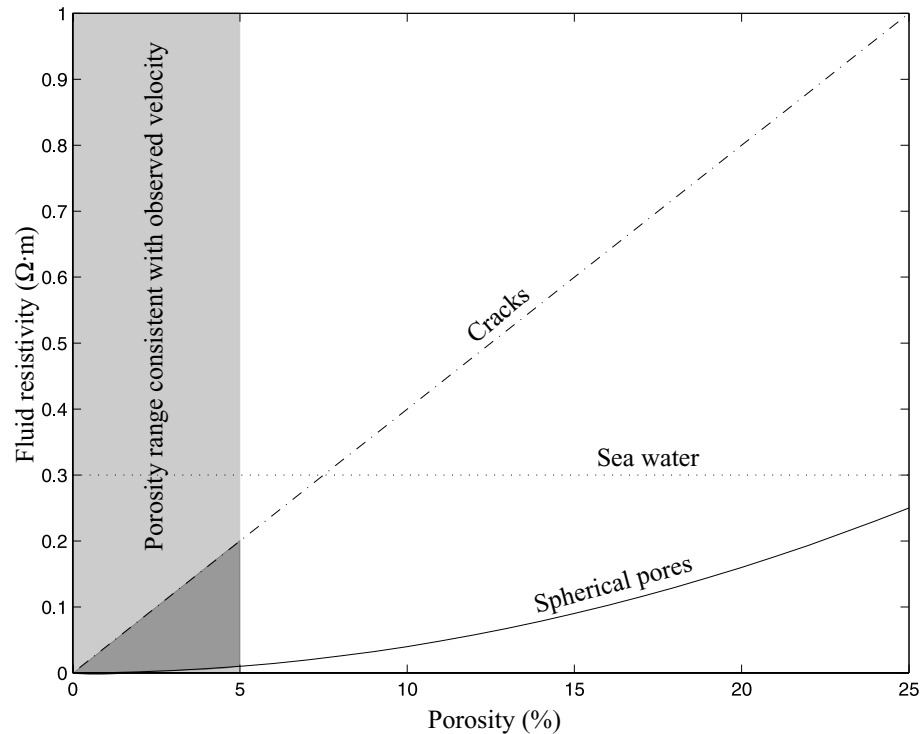


Figure 11. Fluid resistivity/porosity trade-off curves (Archie 1942) corresponding to a bulk resistivity of $4\Omega\ m$, characteristic of class 3 (Table 1). Different curves correspond to fluids distributed in cracks (dashed line) and spherical pores (solid line). The resistivity of sea water is shown for reference. The dark shaded region denotes the approximate range of porosities and fluid resistivities consistent with the data.

geologic units (Table 1). The evidence for this geologic association comes from surface mapping, borehole constraints, and independent geophysical results. The determined class velocities and resistivities are in accordance with the inferred geologic units in all but one case. The Cambrian to Cretaceous sequence equated with classes 3 and 4 is comprised of sandstone, limestone, dolomite and marl. The velocity ($4.4 \pm 0.5\ km\ s^{-1}$) of class 3, the lower half of this sequence, is reasonable for such a heterogeneous package, however the resistivity ($2 - 11\ \Omega m$) is anomalously low. Such low resistivity usually suggests an unusual mineralogy (e.g. graphite or metallic sulfides), chemical/physical weathering, or the presence of a connected fluid phase (Bedrosian 2007). Mineralogy is not a satisfactory explanation, as deeper stratigraphic levels sampled in boreholes show no indication of anomalously conductive mineralogy. Weathering, which can significantly lower a rock's resistivity, is also an unlikely explanation, as it is typically limited to the uppermost hundred meters. Even if exposed in the past, it is unlikely that this ~ 1.5 km thick section has become pervasively weathered.

The most plausible explanation is fluids, which in small percentages can lower rock resistivity dramatically. Fig. 11 illustrates

trade-off curves between fluid resistivity and porosity for two end-member pore geometries (Archie 1942); any combination of fluid resistivity and porosity lying between the two curves is sufficient to produce the bulk resistivity determined for class 3. We are limited to low porosities, however, since beyond a few percent porosity the observed velocity is untenable (velocity is, to first order, inversely proportional to porosity and the modelled velocities are not anomalously low). The fluid hypothesis thus requires that the lithologies comprising class 3 be saturated by a few percent hypersaline ($\rho_f \lesssim 0.2\ \Omega m$) fluid. This is consistent with the observation of saline brines within the Zofar 20 well, situated within the Araba/Arava Valley to the west of the study area.

The presence of fluids within such an extensive zone ($1.5\ km \times >6\ km$) requires a permeable host, structural control, and lastly a source of fluids. The layered sandstones may provide the permeable host, while an overlying chert of Senonian age (up to 200 m thick) may serve as a (relatively) impermeable cap. Faulting likely provides lateral control, as class 3 terminates abruptly along a vertical plane ~ 500 m east of the surface trace of the Araba/Arava Fault. Indeed, Ritter *et al.* (2003) suggest that the AF acts, at least locally, as a barrier to cross-fault fluid flow. Furthermore, our

interpretation of class 2 as Precambrian volcanics and granites suggests a strong permeability contrast exists across the fault. The western boundary of this conductor is located at the edge of the Araba/Arava Rift (O. Ritter, unpubl. data) coincident with the concealed Baraq Fault (Frieslander 1993). It is thus plausible that the lower part of the Cambrian-Cretaceous sequence is host to a hypersaline aquifer within the internally-drained Araba/Arava Rift, bounded by faults to the east and west.

The above structural identification permits several conclusions regarding regional faulting. First, the Araba/Arava Fault cuts cleanly through the subsurface and is subvertical to at least 4 km depth. Furthermore, the lateral change from classes 3, 4, and 5 in the west to class 2 in the east suggests that a fault damage zone, if present, is at most a few hundred meters wide between 0.5 and 3.5 km depth. This is significantly wider than the damage zone observed either from geologic studies (Janssen *et al.*, 2004) or from seismic guided-wave studies by Haberland *et al.* (2003a). It must be noted however, that these studies concern the upper 300 m of the fault in contrast to our deeper estimates.

Second, the AF at depth appears offset to the east by ~ 500 m relative to the surface trace. This finding is supported by the work of Maercklin *et al.* (2004), who image a zone of pronounced seismic scattering ~ 1 km east of the surface trace. Gravity studies by Tasárová *et al.* (2006) also model this offset, and further suggest the connection between the surface trace and the deeper fault to the east occurs within the uppermost 1 km.

Third, the Precambrian rocks (class 1) of the eastern block are offset upward relative to the western block. This may reflect paleotopography, or thickness changes due to the fact that these two blocks originate up to 60 km apart and have been juxtaposed by transform faulting. The local stratigraphy, however, in particular the lack of Eocene and Miocene rocks east of the AF, suggest it represents at least local uplift of the eastern block since the onset of Miocene faulting. Assuming the western block preserves the original thickness of Eocene rocks (and that they were laid down uniformly), this requires a minimum 1 km uplift in order to strip the corresponding sequence from the eastern block. This is in accordance with the ~ 1.3 km offset imaged. Gravity modeling further support this conclusion, with an average vertical basement offset of 1.5 km based off three-dimensional models (Tasárová *et al.* 2006).

Finally, the number of distinct lithologies imaged and their thicknesses are supported by the gravity modeling, suggesting we are

neither artificially subdividing nor grouping distinct lithologies. Excluding the basement, we identified 4 lithologies west of the AF and 2 to the east. The only discrepancy exists in the near-surface layering (classes 1 and 2) east of the AF. As seen in Fig. 2, both the Miocene Hazeva Formation and Quaternary alluvium are exposed at the surface, and are reflected in our results. The gravity modeling groups these into one layer, with a thickness roughly equal to that of the combined classes 1 and 2.

4.2 Methodology

The case study across the Dead Sea transform has identified 6 distinct classes via a statistical classification approach. The fact that classes are well-defined in both the joint parameter space (JPS) and in depth section and furthermore correspond well to independent geologic constraints confirm that we are imaging lithology. Our initial premise was that geologic structures can be more accurately identified and delineated by the increased constraints that multiple data sets provide. All that is required for classification is that the physical parameters characterizing two structures be separable in the JPS.

As an example, take the case of classes 2 and 3, which are characterized by similar (and overlapping) velocities. It is addition of the resistivity information, sensitive to saline pore fluids, that permit a class separation in the JPS, and makes the sharp boundary across the fault apparent. Independent interpretation of the individual models could lead to very different conclusions, while a qualitative comparison would suggest the models are contradictory. As an extreme case, consider the synthetic example shown in Fig. 12. Here, a three-layer earth model is introduced where the middle layer is characterized by a velocity equal to that of the basement and a resistivity identical to the surface layer. Whereas in the case study, the starting point was two inversion models (Figs 3a, c), here the 'true earth' models are used. This is done to highlight aspects of the classification methodology independent of inversion effects, such as regularization, which can leave artifacts in the JPS. For consistency, the synthetic resistivity and velocity models are based upon the same model meshes as in the case study, 5 per cent Gaussian noise has been added to the model parameters, and the interpolation and classification procedures used are identical to that of the case study. In this three-layer case, neither a seismic nor resistivity inversion could correctly recover all three layers. Each would recover a single layer over a halfspace, yet disagree as to the depth to basement. Only when looked at in the JPS (a) do all three layers emerge (b).

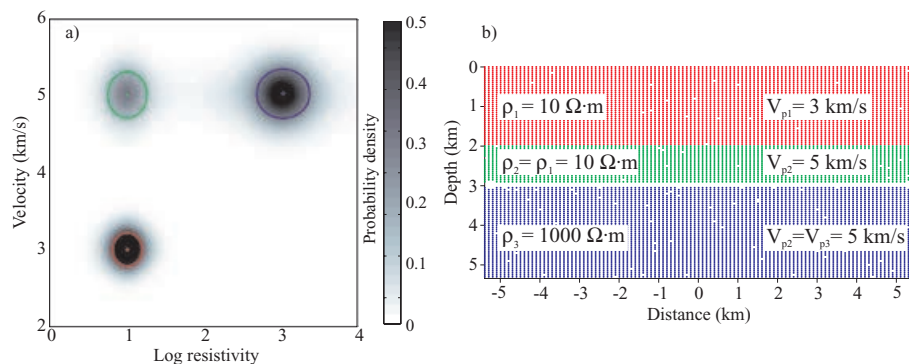


Figure 12. Joint probability density function (a) and spatial distribution of selected classes (b) for a synthetic three-layer earth model. Class boundaries in (a) denote the 60 per cent confidence interval for each of the classes determined via automatic fitting of the pdf. Portions of the joint parameter space interior to these colored boundaries are represented in the spatial domain (b) by corresponding colors.

Though this example presents an extreme case, it highlights several points. The synthetic example reveals three classes cleanly separated in the joint parameter space. The spread of the classes in the JPS reflects the variability within the class, in this case recovering the 5 per cent Gaussian noise added to the initial layer velocities and resistivities. In our real data example, the elongated confidence intervals suggest that a class is more tightly constrained in one parameter than the other. Class 1, for example is characterized by a narrow range in velocity (± 5 per cent) and a wider range in log resistivity (± 24 per cent).

For a given class, the peak probability density reflects not only how well-correlated the model parameters are, but also the relative errors in the model parameters and finally, the spatial extent of the individual class. In the synthetic example, velocity and resistivity are equally well-correlated throughout the model and a uniform error distribution has been assumed. It is the differing spatial extent of the three classes which gives rise to a smaller peak probability density for the thin intermediate layer relative to the thicker layers above and below. Similarly, class 1 in the case study exhibits the highest peak probability density (Fig. 8). Looking at the model section (Fig. 10), class 1 comprises roughly half of the analyzed model area, with the remaining area split among the other 5 classes. To avoid one class obscuring others in the JPS (note the overlap between classes 1 and 2 in Fig. 8) care must be taken in choosing the area of analysis. While normalizing the pdf by class area during its construction seems an attractive possibility, it must be remembered that class areas are not known *a priori*, but only following classification.

The lack of a connection between the classes in the JPS suggests a sharp boundary exists between the individual layers in the spatial domain. This is in contrast to our real data example, where 'bridges' can be seen connecting several of the classes in the JPS. The bridges are suggestive of smooth boundaries or diffuse material gradients between the classes. While such behavior may reflect the real earth, it is commonly the result of the smoothing regularization in the inversion algorithms. By examining the bridges radiating from a single class, it is possible to quickly assess which classes are adjacent to it in the spatial domain. Class 4, for example, can be seen to be in contact with the overlying class 5, the underlying class 3, and the abutting class 2.

The gradients between classes can be exploited to provide a structural linkage in joint inversion algorithms. Joint inversion has typically proceeded via empirical or theoretical linkages between the physical parameters being inverted for. These linkages, however, may only be applicable over a narrow region of the joint parameter space, are limited to a particular pressure/temperature range, or are complicated by unaccounted for secondary dependencies such as pore saturation and pore aspect ratio. Model structure linkages thus provide a less restrictive regularization to the inverse problem that still honors the individual data sets. Recent work by Gallardo & Meju (2004) details a joint inversion methodology employing the cross-product of resistivity and velocity gradients to provide such a structural linkage. The cross-product seeks to minimize non-parallel structure, or alternatively to bring out colinear gradients; these colinear gradients are the bridges we observe connecting our classes. The technique of Gallardo & Meju (2004) succeeds in increasing the structural conformity of the resulting resistivity and velocity models without forcing or assuming a relationship between these parameters. The results of the classification approach presented here offer an alternative means with which to regularize a joint inversion. Based on spatial class boundaries, an inversion could be formulated so as to limit its search to the corresponding subregion of the joint parameter space.

5 CONCLUSION

This study has outlined a quantitative, statistical approach to structure classification based on the joint interpretation of magnetotelluric and seismic models. The method rests upon the underlying assumption of all geophysics – that geologic units are characterized by their physical properties, and can be distinguished through indirect measurement of these properties. Distinct structures can thus be distinguished provided their separation in parameter space is greater than the variation of physical parameters within a structure.

When presented with coincident, independently-derived physical property models, statistical correlation can be used as a basis for a joint quantitative interpretation. The method employed consists of (1) interpolation of models onto a common mesh, (2) construction of a probability density function describing the physical parameter distribution, (3) identification of classes and class boundaries in the joint parameter space, and (4) mapping of class inclusions onto the original depth sections.

The method is independent of theoretical/empirical relations linking electrical and seismic parameters. It represents an advance from the common qualitative interpretation of multiple physical property models, and is less susceptible to the subjectivity of such a joint interpretation. It likewise is more tractable than a joint inversion in that it operates on post-inversion models, eliminating reanalysis of the data. As shown in a synthetic example, our approach is capable of 'breaking the degeneracy' of overlapping physical parameters, providing structural information not evident in the individual models.

This approach has been applied to magnetotelluric and seismic model sections spanning the Araba/Arava Fault in Jordan, providing a clear delineation of stratigraphy in accordance with independent geologic results. Classes identified in the joint parameter space, with boundaries defined by confidence ellipses, are found to correspond to spatially well-connected regions in depth section, validating the initial assumption. The classes and boundaries are derived from both the initial models, and are not evident from either model alone. From a methodological viewpoint, this approach highlights the structural conformity of the models, and provides a natural means for regularization of a joint inversion.

ACKNOWLEDGMENTS

We thank the National Ministry of Infrastructure of Israel, the Natural Resources Authority of Jordan and the An-Najah National University in Nablus, Palestine, for their support. The instruments were provided by the Geophysical Instrument Pool of the GeoForschungsZentrum Potsdam (GFZ). The experiments were funded by the Deutsche Forschungsgemeinschaft and the GFZ. This manuscript has benefitted greatly from suggestions by the DESERT Working Group, Luis Gallardo, and one anonymous reviewer. PAB was supported by the Alexander von Humboldt Foundation.

REFERENCES

- Amiran, D., Arie, E. & Turcotte, T., 1994. Earthquakes in Israel and adjacent areas: macroseismic observations since 100 B.C.E., *Israel Explor. J.*, **44**, 260–305.
- Archie, G., 1942. The electrical resistivity log as an aid in determining some reservoir characteristics, *Trans. Am. Inst. Min. Metall. Pet. Eng.*, **146**, 54–62.
- Armstrong, M., 1998. *Basic Linear Geostatistics*, Springer-Verlag Press, Berlin.

- Bartov, Y., Steinitz, G., Eyal, M. & Eyal, Y., 1980. Sinistral movement along the Gulf of Aqaba- its age and relations to the opening of the Red Sea, *Nature*, **285**, 220–222.
- Bauer, K., Schulze, A., Ryberg, T., Sobolev, S. & Weber, M., 2003. Classification of lithology from seismic tomography: a case study from the Mesum igneous complex, Namibia, *J. Geophys. Res.*, **108**, doi:10.1029/2001JB001073.
- Bedrosian, P., Unsworth, M., Egbert, G. & Thurber, C., 2004. Geophysical images of the creeping San Andreas Fault: Implications for the role of crustal fluids in the earthquake process, *Tectonophysics*, **358**, doi:10.1016/j.tecto.2004.02.010.
- Bedrosian, P.A., MT+, Integrating Magnetotellurics to Determine Earth Structure, Composition, and Processes, *Surveys in Geophysics*, p. in review, 2007.
- Bender, F., 1968. *Geologie von Jordanien*, Vol. 7 of *Beiträge zur regionalen Geologie der Erde*, Gebrüder Borntraeger, Berlin, Stuttgart.
- Bosch, M., 1999. Lithologic tomography: from plural geophysical data to lithology estimation, *J. Geophys. Res.*, **104**, 749–766.
- Bosworth, W., Guiraud, R. & Kessler, L., 1999. Late Cretaceous (ca. 84 Ma) compressive deformation of the stable platform of north-east Africa (Egypt): Far-field stress effects of the ‘Santonian event’ and origin of the Syrian arc deformation belt, *Geology*, **27**, 633–636.
- Dell’Aversana, P., 2001. Interpretation of seismic, MT and gravity data in a thrust belt interpretation, *First Break*, **19**, 335–341.
- DESERT Research Group, 2000. Multinational Geoscientific Research Effort Kicks Off in the Middle East, *Eos, Transactions, American Geophysical Union*, No. 50, December 12, **81**, 609, 616–617.
- Freund, R., Garfunkel, Z., Zak, I., Goldberg, M., Derin, B. & Weissbrod, T., 1970. The shear along the Dead Sea rift, *Phil. Trans. R. Soc.*, **267**, 107–130.
- Frieslander, U., 1993. Semi-high resolution seismic surveys in the central Arava, *Inst. Petrol. Res. Geophys. Rep.* 946/257/92, p. 10 pp., in Hebrew.
- Gallardo, L. & Meju, M.A., 2004. Joint two-dimensional DC resistivity and seismic travel time inversion with cross-gradients constraints, *J. Geophys. Res.*, **109**, doi:10.1029/2003JB002716.
- Gallardo, L.A. & Meju, M.A., 2003. Characterization of heterogeneous near-surface materials by joint 2D inversion of dc resistivity and seismic data, *Geophys. Res. Lett.*, doi:10.1029/2003AL017370.
- Gallardo, L.A. & Meju, M.A., 2007. Joint two-dimensional cross-gradient imaging of seismic traveltime data for structural and lithological classification, *Geophys. J. Int.*, doi:10.1111/1365-246X.2007.03366.x.
- Garfunkel, Z., Zak, I. & Freund, R., 1981. Active faulting in the Dead Sea rift, *Tectonophysics*, **80**, 1–26.
- Haber, E. & Oldenburg, D., 1997. Joint inversion: a structural approach, *Inverse Problems*, **13**, 63–77.
- Haberland, C. et al., 2003a. Modeling of seismic guided waves at the Dead Sea Transform, *J. Geophys. Res.*, **108**, doi:10.1029/2002JB002309.
- Haberland, C., Rietbrock, A., Schurr, B. & Brasse, H., 2003b. Coincident anomalies of seismic attenuation and electrical resistivity beneath the southern Bolivian Altiplano plateau, *Geophys. Res. Lett.*, **30**, doi:10.1029/2003GL017492.
- Ibrahim, K. & McCourt, W., 1995. Neoproterozoic granite magnetism and tectonic evolution of the northern Arabian Shield: evidence from south-west Jordan, *J. Afr. Earth Sci.*, **20**, 103–118.
- Isaaks, E. & Srivastava, R., 1989. *An Introduction to Applied Geostatistics*, Oxford University Press, New York.
- Janssen, C., Romer, R., Hoffmann-Rothe, A., Kesten, D., Al-Zubi, H. & Group, D., 2004. The Dead Sea Transform: evidences for a strong fault?, *Journal of Geology*, **12**, 561–575.
- Jones, A., 1987. MT and reflection: an essential combination, *Geophys. J. R. Astron. Soc.*, **89**, 7–18.
- Kesten, D., Weber, M., Haberland, C., Janssen, C., Agnon, A., Bartov, Y., Rabba, I. & the DESERT GROUP, 2007. Combining satellite and seismic images to analyze the shallow structure of the Dead Sea Transform near the DESERT transect, *Int. J. Earth Sci.*, doi:10.1007/s00531-006-0168-5.
- Klinger, Y., Avouac, J., Karaki, N.A., Dorbath, L., Bourles, D. & Reyss, J., 2000. Slip rate on the Dead Sea transform in northern Araba Valley (Jordan), *Geophys. J. Int.*, **142**, 755–768.
- Linde, N., Binley, A., Tryggvason, A., Pedersen, L.B. & Revel, A., 2006. Improved hydrogeographical characterization using joint inversion of cross-hole electrical resistance and ground-penetrating radar traveltime data, *Water Resources Res.*, **42**, doi:10.1029/2006WR005131.
- Maercklin, N., 2004. *Seismic structure of the Arava Fault, Dead Sea Transform*, PhD thesis, University of Potsdam, Germany, <http://pub.ub.uni-potsdam.de/2004meta/0046/door.htm>.
- Maercklin, N., Haberland, C., Ryberg, T., Weber, M., Bartov, Y. & Group, D., 2004. Imaging the Dead Sea Transform with scattered seismic waves, *Geophys. J. Int.*, **158**, 179–186.
- Maercklin, N., Bedrosian, P.A., Haberland, C., Ritter, O., Ryberg, T., Weber, M. & Weckmann, U., 2005. Characterizing a large shear-zone with seismic and magnetotelluric methods: The case of the Dead Sea Transform, *Geophys. Res. Lett.*, **32**, doi:10.1029/2005GL022724.
- Niemi, T., Zhang, H., Atallah, M. & Harrison, B., 2001. Late Pleistocene and Holocene slip rate of the Northern Wadi Araba fault, Dead Sea Transform, Jordan, *J. Seismol.*, **5**, 449–474.
- Ritter, O., Junge, A. & Dawes, G., 1998. New equipment and processing for magnetotelluric remote reference processing, *Geophys. J. Int.*, **132**, 535–548.
- Ritter, O., Ryberg, T., Weckmann, U., Hoffmann-Rothe, A., Abueladas, A., Garfunkel, Z. & DESERT Research group, 2003. Geophysical images of the Dead Sea Transform in Jordan reveal an impermeable barrier for fluid flow, *Geophys. Res. Lett.*, **30**, doi:10.1029/2003GL017541.
- Rodi, W. & Mackie, R.L., 2001. Nonlinear conjugate gradients algorithm for 2D magnetotelluric inversion, *Geophysics*, **66**, 174–187.
- Schalkoff, R., 1992. *Pattern Recognition: Statistical, Structural, and Neural Approaches*, John Wiley and Sons, New York, pp. 364.
- Schwalenberg, K., Rath, V. & Haak, V., 2002. Sensitivity studies applied to a two-dimensional resistivity model from the Central Andes, *Geophys. J. Int.*, **150**, 673–686.
- Stern, R., 1994. Arc assembly and continental collision in the neoproterozoic East African orogen: implications for the consolidation of Gondwanaland, *Ann. Rev. Earth and Planet. Sci.*, **22**, 319–351.
- Stoeser, D. & Camp, V., 1985. Pan-African microplate accretion of the Arabian Shield, *Geological Society of America Bulletin*, **96**, 817–826.
- Tasárová, Z., Göetze, H.J., El-Kelani, R., Ebbing, J. & Hassounch, M., 2006. Small-scale gravity modeling of upper-crustal structures in the Araba Valley along the Dead Sea Transform, *G3*, **7**, doi:10.1029/2005GC001229.
- van Eck, T. & Hofstetter, A., 1990. Fault geometry and spatial clustering of microearthquake along the Dead Sea-Jordan rift fault zone, *Tectonophysics*, **180**, 15–27.
- Vozoff, K., 1987. The magnetotelluric method, in *Electromagnetic Methods in Applied Geophysics*, ed. Naibighian, M., pp. 641–711, Society of Exploration Geophysics, Tulsa, OK.
- Weber, M. et al., 2004. The crustal structure of the Dead Sea Transform, *Geophys. J. Int.*, **156**, 655–681.
- Weckmann, U., Magunia, A. & Ritter, O., 2005. Effective noise separation for magnetotelluric single site data processing using a frequency domain selection scheme, *Geophys. J. Internat.*, **161**, 456–468.
- Weissbrod, T. & Sneh, A., 2002. Sedimentology and paleogeography of the late Precambrian-early Cambrian arkosic and conglomeratic facies in the northern margins of the Arabo-Nubian Shield, *Geologic Survey of Israel, Bulletin*, **87**, p. 44.
- Zelt, C.A. & Barton, P.J., 1998. Three-dimensional seismic refraction tomography: A comparison of two methods applied to data from the Faeroe Basin, *J. Geophys. Res.*, **103**, 7187–7210.